ACS APPLIED MATERIALS & INTERFACES
Research Article
www.acsami.org

Silver–Copper Nanoalloy Catalyst Layer for Bifunctional Air Electrodes in Alkaline Media

Xiaoqiang Wu,[†] Fuyi Chen,[*,†] Yachao Jin,[†] Nan Zhang,[†] and Roy L. Johnston[*,‡]

[†]State Key Laboratory of Solidification Processing, Northwestern Polytechnical University, Xian 710072, China
[‡]Department of Chemistry, University of Birmingham, Birmingham B15 2TT, United Kingdom

Supporting Information

ABSTRACT: A carbon-free and binder-free catalyst layer composed of a Ag–Cu nanoalloy on Ni foam was used as the air cathode in a zinc–air battery for the first time. The Ag–Cu catalyst was prepared using pulsed laser deposition. The structures of the catalysts were found to consist of crystalline Ag–Cu nanoalloy particles with an average size of 2.58 nm embedded in amorphous Cu films. As observed in the X-ray photoelectron spectra, the Ag 3d core levels shifted to higher binding energies, whereas the Cu 2p core levels shifted to lower binding energies, indicating alloying of the silver and copper. Rotating disk electrode measurements indicated that the oxygen reduction reaction (ORR) proceeded through a four-electron pathway on the $Ag_{50}Cu_{50}$ and $Ag_{90}Cu_{10}$ nanoalloy catalysts in alkaline solution. Moreover, the catalytic activity of $Ag_{50}Cu_{50}$ in the ORR is more efficient than that of $Ag_{90}Cu_{10}$. By performing charge and discharge cycling measurements, the $Ag_{50}Cu_{50}$ catalyst layer was confirmed to have a maximum power density of approximately 86.3 mW cm^{-2} and an acceptable cell voltage at 0.863 V for current densities up to 100 mA cm^{-2} in primary zinc–air batteries. In addition, a round-trip efficiency of approximately 50% at a current density of 20 mA cm^{-2} was also obtained in the test.

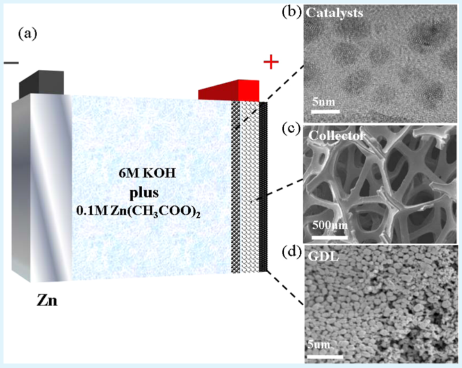

KEYWORDS: *nanoalloy, pulsed laser deposition, oxygen reduction reaction, primary zinc–air battery, rechargeable zinc–air battery*

INTRODUCTION

Metal–air batteries based on oxygen reduction and evolution reactions in alkaline media, such as zinc–air,[1] magnesium–air,[2] and lithium–air batteries,[3] are of considerable interest because of their numerous advantages. Compared to state-of-the-art Li-ion batteries, metal–air batteries always possess high theoretical specific energies, good safety records, and low costs, and these batteries do not pollute. Similar to fuel cells, the air cathodes in metal–air batteries include a gas diffusion layer and can obtain oxygen from the surrounding environment rather than requiring storage in the device. However, a critical technological challenge for the commercialization of these types of metal–air batteries is the development of high-performance and cost-effective air electrodes, which require low overpotentials to drive the oxygen reduction reaction (ORR) and oxygen evolution reaction (OER).[4−6]

Air electrodes are generally composed of a gas diffusion layer, a collector, and a catalyst layer that includes carbon, such as Ag/C, Pd–TiO_2/C, or Pt/C.[7−10] This approach has an inherent disadvantage because carbon is readily corroded at the highly oxidative electrochemical potentials encountered during the oxidation of water, which will reduce the amount of catalytic material on the air cathode. The ORR catalyst is another key factor that influences the overall performance of metal–air batteries. The ORR on air cathodes is a complicated reaction with slow kinetics in either acidic or alkaline solutions. In general, Pt and Pt-based alloys are the most efficient catalysts for the ORR. However, their prohibitive cost restricts their application in various electrochemical technologies. Therefore, it is highly desirable to explore novel catalysts, such as Co-based catalysts,[11−13] Fe-based catalysts,[14,15] Mn-based catalysts,[16,17] and Ag-based catalysts,[18−21] to replace the expensive Pt-based catalysts in the development of air cathodes.

For ORR catalysis in alkaline electrolytes, the reduction of O_2 can proceed through one of two pathways. The first pathway is the direct reduction of O_2 to OH^- ions, which is known as the four-electron pathway (1), and the second pathway is the reduction of O_2 to HO_2^- ions, which is known as the two-electron pathway (2):[7]

$$O_2 + 2H_2O + 4e^- \rightarrow 4OH^- \quad (1)$$

$$O_2 + H_2O + 2e^- \rightarrow HO_2^- + OH^- \quad (2)$$

The kinetics and mechanisms of O_2 reduction are highly dependent on the selected catalyst. Due to its similar ORR mechanism to Pt catalysts (four-electron pathway), Ag is a competitive ORR catalyst and has a reasonably high catalytic activity for the reduction of O_2 in alkaline electrolytes. However, the energy adsorption of O_2 on pure Ag particles is small, leading to relatively low catalytic activity. Therefore,

Received: May 11, 2015
Accepted: July 22, 2015
Published: July 22, 2015

DOI: 10.1021/acsami.5b04061

doping or alloying Ag catalysts has been proposed to overcome this problem.[22]

Ag−Cu alloys are considered to be efficient air cathode catalysts for metal−air batteries.[23,24] Our previous work using first-principles calculations indicates that the energies for the adsorption of O_2 on Ag and Cu are 0.6 and 1.76 eV, respectively, whereas the absorption energy for the Ag−Cu alloy is between these values, indicating that the alloy possesses more efficient ORR activity than that of pure Ag catalysts.[22] However, to the best of our knowledge, no experimental studies on Ag−Cu catalysts in metal−air batteries have been reported.

In this work, Ag−Cu nanoalloys were directly deposited on nickel foams using pulsed laser deposition (PLD). The thin film was used as the catalyst layer of the air cathode for a single zinc−air battery and was found to exhibit good bifunctional catalytic performance. The effect of the Ag/Cu atomic ratio on the average electron transfer numbers in the ORR was systematically investigated. For the first time, this carbon-free and binder-free bimetallic catalyst layer was found to possess both ORR and OER catalytic activity in rechargeable zinc−air batteries.

EXPERIMENTAL SECTION

Preparation and Characterization. Ag−Cu nanoalloys were directly deposited on nickel foam using PLD. Several target Ag−Cu alloys with Ag/Cu atomic ratios of 90:10, 50:50, 75:25, and 25:75 were used. The substrates were prepared using high-purity (99.97%) nickel foam, followed by soaking in acetone for 3 h and 10% H_2SO_4 for 15 min, washing in distilled water for 10 min, and drying under vacuum for 2 h. The targets were irradiated using a nanosecond Q-switched Nd:YAG laser (EKSPLA, Lithuania) with a wavelength of 266 nm, pulse duration of 3−6 ns, beam diameter of 1 mm, and energy density of 200 mJ/pulse. To remove the oxides from the target, the laser frequency was set at 1 Hz and the substrate-to-target distance was set to 5 cm at the beginning of the process. During the deposition process, the laser frequency was set to 10 Hz to deposit the Ag−Cu nanoalloy on the nickel foam with 36000 laser pulses, and the target and substrate were both rotated at 5 rpm. For all samples, the catalyst loading was 0.113 mg cm^{-2} $Ag_{50}Cu_{50}$ alloy catalyst, which was calculated from the film thickness of 120 nm. The gas diffusion layer was prepared using a mixture of 0.5 g of acetylene black, 2.5 mL of PTFE (65%) and 15 mL of absolute ethanol. This mixture was stirred for approximately 3 h, ultrasonically separated for approximately 15 min, and heated in a water bath for approximately 10 min at 80 °C. Finally, the air diffusion layer was fitted on the back of the catalyst layer and pressed into 0.5 mm thick layers under a pressure of 10 MPa.

The structural and electronic properties of the synthesized catalysts were determined using an FEI Tecnai F30 transmission electron microscope (200 kV), a JEOL JSM-6700F field-emission scanning electron microscope, and an ESCALAB 250 X-ray photoelectron spectrometer (XPS) with a monochromic Al Kα X-ray source (E = 1486.6 eV).

Electrochemical Measurements. All electrochemical measurements were performed using a CHI660C electrochemical workstation in a classic three-electrode cell with a saturated calomel electrode (SCE) as the reference electrode, a Pt counter electrode, and a working electrode fabricated using the Ag−Cu catalysts. The electrocatalytic activities of the catalysts were investigated at room temperature using linear sweep voltammetry (LSV) and rotating disk electrode (RDE) polarization curves obtained in a 0.1 M KOH aqueous solution. The experiments were performed over the potential range of 0 to −0.8 V at a scan rate of 10 mV s^{-1}. The rotation rates were controlled at 400, 800, 1600, 2400, and 3200 rpm.

For the batteries, the working area of the air electrode was 0.785 cm^2, and the anode was a zinc plate. For the primary batteries, the alkaline electrolyte was a 6.0 M KOH aqueous solution, whereas the alkaline electrolyte was a 6.0 M KOH + 0.1 M $Zn(CH_3COO)_2$ aqueous solution for the rechargeable batteries. The performances of the zinc−air batteries were measured using a TC 5.X battery testing system (Neware Co., Shenzhen, China), and the gas evolution was measured using gas chromatography (GC7980) with thermal conductivity detection (TCD).

RESULTS AND DISCUSSION

Figure 1 and Supporting Information Figure S1 present microscopy images of the $Ag_{50}Cu_{50}$ catalyst used in this work.

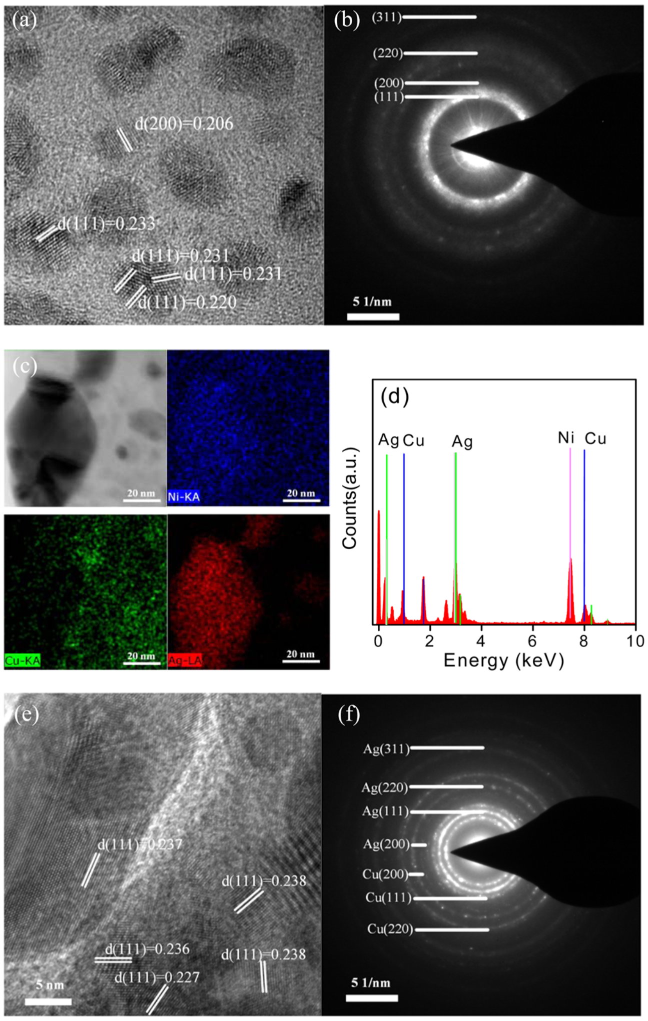

Figure 1. (a) HRTEM images of the $Ag_{50}Cu_{50}$ prepared by PLD. (b) Selected area diffraction patterns for initial Ag−Cu NPs. (c) Bright-field TEM image of Ag−Cu alloy nanoparticle with corresponding Ag, Cu, and Ni Kα EDS signals. (d) EDS of the $Ag_{50}Cu_{50}$ film on nickel grid. (e) HRTEM images of the Ag−Cu after 200 cycles. (f) Selected area diffraction patterns after 200 cycles.

The diameter distribution of the Ag−Cu nanoparticles is from 1 to 5 nm, and the average diameter is approximately 2.58 nm. Bright-field transmission electron microscopy investigation reveals the presence of Ag−Cu crystallites in the substrate, with lattice planes ranging from 0.220 to 0.231 nm indexed to (111) face-centered cubic planes (Ag-rich). The selected area electron diffraction (SAED) pattern shows five diffuse halos, thus providing further evidence that the Ag−Cu nanoparticles are polycrystalline, as shown in Figure 1b. Furthermore, as shown in Figure S1c, the quantitative EDS line scanning analysis indicates that the average atomic ratio of the Ag−Cu

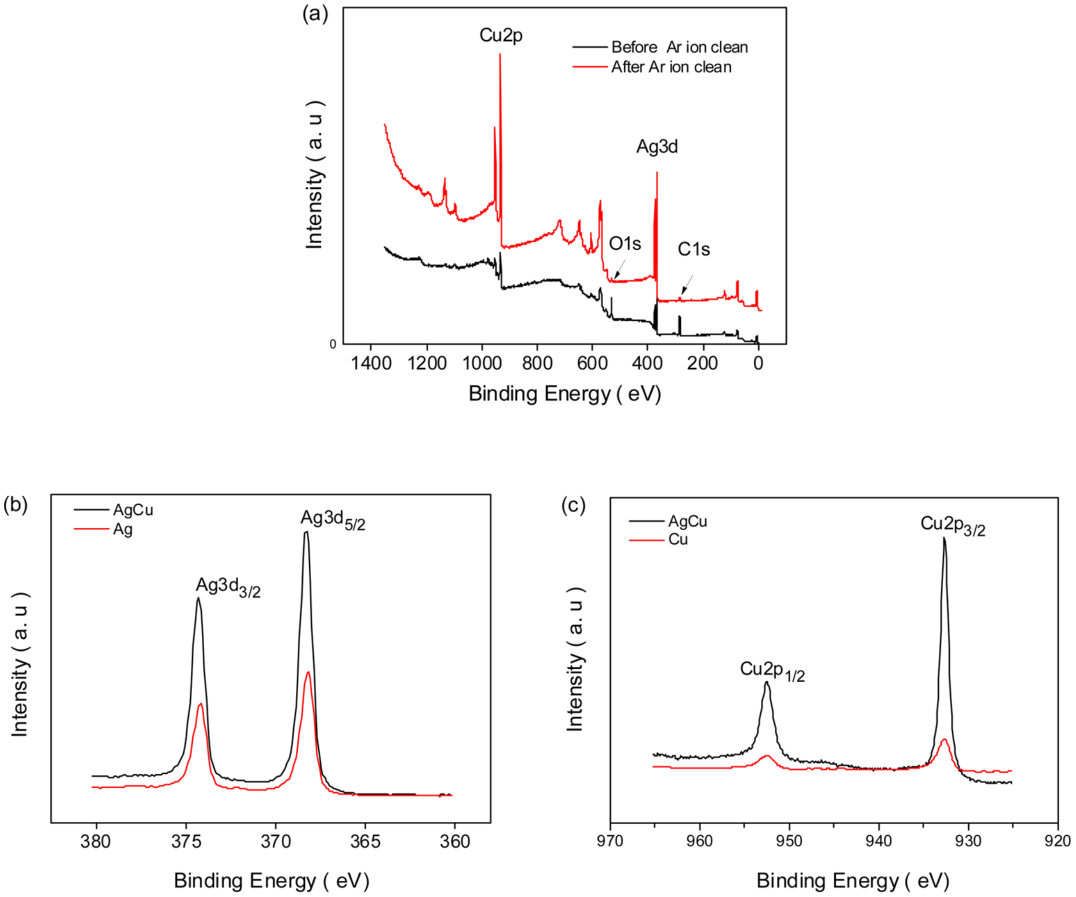

Figure 2. XPS spectra of $Ag_{50}Cu_{50}$ catalysts supported on Ni foam: (a) full spectra of Ag and Cu element; (b) Ag 3d regions; (c) Cu 2p regions.

NPs is approximately 80:20 (Ag to Cu) and reveals the Ag atoms are enriched in the surface alloy shell.

The high-resolution TEM images and corresponding elemental mapping, as shown in Figure 1c,d, indicate that the nanoparticles are enriched with Ag atoms, whereas the film is enriched with Cu atoms. Thus, the nanocatalyst layer is composed of Ag-enriched nanoparticles and an amorphous Cu-enriched film. According to a previous study, these Cu-doped Ag nanoparticles are predicted to exhibit higher catalytic performance than pure Ag nanoparticles because the doping of Cu in Ag nanoparticles may move the d-band center toward the Fermi level, thereby improving the O_2 adsorption energy and reducing the dissociation energy of O_2 on the surfaces of the nanoparticles.[23] This question is studied later in this work. The Ag-based electrocatalysts in the amorphous films may be created from the vapor phase under far-from-equilibrium conditions using PLD. Previous work demonstrated that face-centered cubic Ag−Cu solid solutions or completely amorphous Ag−Cu metal glasses, such as corrosion-resistant nonequilibrium alloys or metastable phases, were formed by rapid quenching from the liquid or vapor phase.[25]

To investigate the effects of charging and discharging on the Ag−Cu catalysts, the patterns after 200 cycles were measured using TEM, as shown in Figure 1e,f and Figure S1b. The high-resolution TEM image in Figure 1e shows that the Ag−Cu nanocrystals have lattice fringe spacings that range from 0.227 to 0.238 nm, which are indexed as the (111) planes of the face-centered cubic structure. Compared to the initial samples (Figure 1a), these nanoparticles are larger than the initial particles, indicating that the nanoparticles underwent a growth process. Figure 1f presents the SAED pattern of the Ag−Cu catalysts after 200 cycles, which shows more diffraction rings than that of the initial Ag−Cu nanoparticles. For this sample, seven diffuse halos are observed and can be identified as the Ag(111), Ag(200), Ag(220), Ag(311), Cu(111), Cu(200), and Cu(220) planes. Compared to Figure 1b, these Cu planes suggest that Cu-rich crystalline grains are generated during the charging and discharging processes. These results indicate AgCu crystalline grains are separated and formed AgCu(Ag-rich) crystalline grains and AgCu(Cu-rich) crystalline grains during operation.

To analyze the specific surface composition of the Ag−Cu catalysts, X-ray photoelectron spectroscopy was employed to acquire information about the interaction of Ag with Cu. Figure 2a presents the full XPS spectra of the $Ag_{50}Cu_{50}$ catalysts on the nickel foam, which was cleaned using Ar ions or not cleaned. The peak values of oxygen and carbon, at 530.86 and 285.05 eV, both decreased after treatment. Moreover, both of the binding energies were lower than their zerovalent (O^0 or C^0) values, indicating that O_2 and C were chemisorbed on the surface.

Parts b and c of Figure 2 present detailed scans of Ag 3d and Cu 2p in the $Ag_{50}Cu_{50}$, and pure Ag and Cu catalysts on nickel foam. The Ag 3d core level from the pure Ag has two peaks at 368 and 374 eV, which are attributed to metallic silver (Ag^0). A significant positive shift (ca. 0.27 and 0.37 eV) of the binding energy for Ag 3d relative to the $Ag_{50}Cu_{50}$ (ca. 368.27 and 374.37 eV) is identified, which is attributed to the contact between Ag and Cu. Moreover, the zerovalent O state (O^0) after ion cleaning indicated that this shift is not affected by Cu

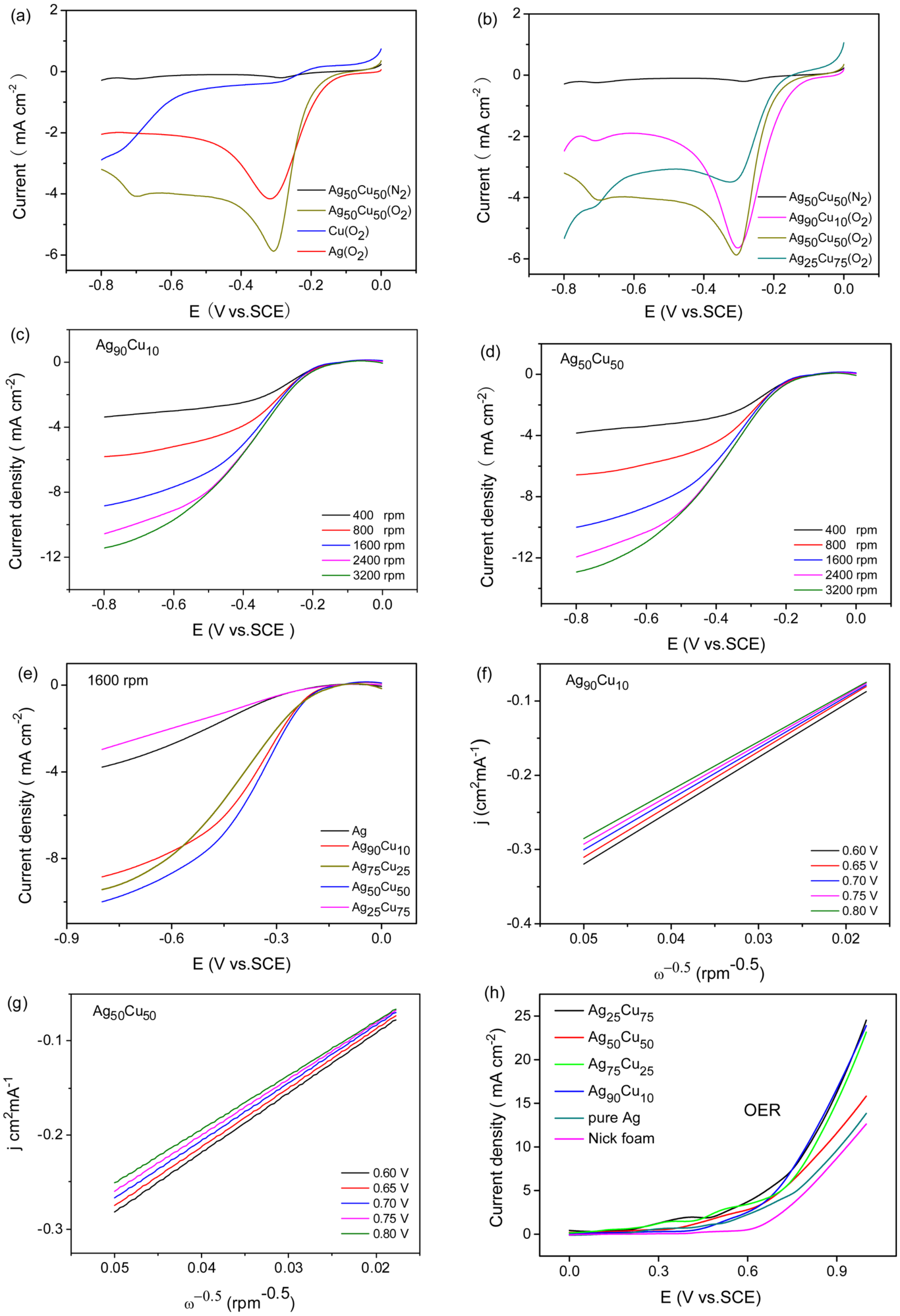

Figure 3. (a) LSV curves of pure Ag, Cu, and $Ag_{50}Cu_{50}$ nanoalloys at a scan rate of 10 mV/s. The electrolyte is N_2 or O_2 saturated 0.1 M KOH solution. (b) LSV curves of $Ag_{90}Cu_{50}$, $Ag_{50}Cu_{50}$, and $Ag_{25}Cu_{75}$ nanoalloys at scan rate of 10 mV/s. (c, d) RDE polarization curves of $Ag_{90}Cu_{50}$ and $Ag_{50}Cu_{50}$ nanoalloys at different rotating rates. (e) RDE polarization curves of Ag, $Ag_{90}Cu_{50}$, $Ag_{75}Cu_{25}$, $Ag_{50}Cu_{50}$, and $Ag_{25}Cu_{75}$ nanoalloys at 1600 rpm. (f, g) Koutecky−Levich plots collected from corresponding RDE polarization curves. (h) Linear sweep voltammogram (LSV) displaying oxygen evolution activities of nickel foam, $Ag_{25}Cu_{75}$, $Ag_{50}Cu_{50}$, $Ag_{75}Cu_{25}$, $Ag_{90}Cu_{10}$, and pure Ag electrodes.

or Ag oxides, such as AgO or Ag_2O. Similar positive chemical shifts for Ag 3d orbitals have been observed in Ag-based intermetallic compounds, such as Ag_4Sn/C (368.65 and 374.65 eV) and Ag_3Mg (368.30 and 374.30 eV), and for Ag-based solid solutions, such as $Ag_{75}Au$ (Ag $3d_{5/2}$ at 368.30 eV).[26−28] However, the Ag 3d binding energy shifts are negative in the Ag−Pd and Ag−Pt systems, which is in agreement with the electronegativity argument.[29] Previous discussions suggested

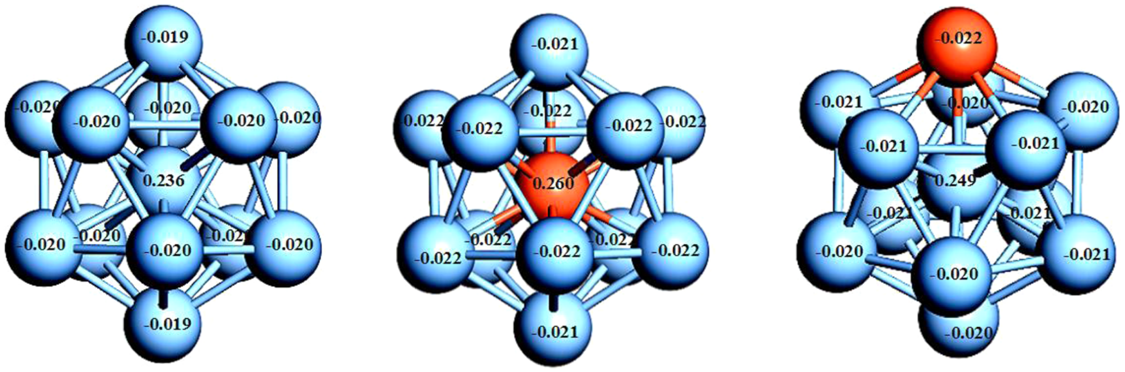

Figure 4. Mulliken atomic charge of the Ag_{13}, $Ag_{12}Cu$(Cu-core), and $Ag_{12}Cu$(Cu-shell) structures.

that charge re-distribution does not occur in the Ag−Cu system according to this rule. Thus, based on our experimental observations, the Ag and Cu are well alloyed in the nanoparticles, which are embedded in the amorphous film. Both alloyed[30] and core−shell[31] Ag−Cu nanoparticles have been synthesized using PLD.

The high-resolution spectra of the Cu levels from pure Cu and $Ag_{50}Cu_{50}$ are shown in Figure 2c. The Cu 2p binding energies from pure Cu are 953 and 933 eV, which are the same as the values reported in the literature.[32] A significant negative shift (ca. 0.53 and 0.33 eV) of the binding energy for Cu 2p relative to 952.47 and 932.67 eV is identified in the $Ag_{50}Cu_{50}$ catalyst, and there is no CuO coverage on the surface. Thus, the shifts in the Ag 3d and Cu 2p binding energies in the $Ag_{50}Cu_{50}$ catalysts are due to the electronic interactions between the Ag and Cu atomic orbitals. One pathway is some degree of charge donation from Ag to Cu, leading to higher Ag 3d and lower Cu 2p binding energies relative to those of pure Ag and Cu, respectively, similar to the Ag $3d_{5/2}$ and Cu $2p_{3/2}$ of the clean Ag−Cu eutectic alloy (ca. 368.5 and 932.3 eV).[33] The other pathway is electronic interactions between the surface atoms and the core atoms, where the electrons transfer from the surface atom site to the core atom site, as reported based on our previous calculations.[34]

The high-resolution spectra of Cu and Ag show that Ag and Cu atoms exist in the metallic form. For the bimetallic catalyst, there are no metal atoms in the oxidized state, and no Ni binding energy peaks are observed in the XPS curves, indicating that the Ag and Cu atoms are well distributed and completely cover the nickel foam. The Ag and Cu atoms form an alloy on the surface of the $Ag_{50}Cu_{50}$ catalyst, and the electron re-distribution plays a key role in the alloying tendencies of heterogeneous Ag−Cu systems. As shown in Figure 1, the laser-deposited catalysts possess a large Cu−Ag *d*-spacing. Additionally, the electronic interactions between the core atoms and the shared atoms at the interface contribute to the nanoalloying between the Ag and Cu atoms.

The LSV curves of pure Ag and the bimetallic Ag−Cu catalysts were recorded in 0.1 M KOH solutions saturated with N_2 or O_2. Parts a and b of Figure 3 present the LSV curves of the pure Ag, $Ag_{90}Cu_{10}$, $Ag_{50}Cu_{50}$, $Ag_{25}Cu_{75}$, and pure Cu catalysts. Cathodic reduction current peaks are clearly observed in the O_2-saturated solutions but not in the N_2-saturated solutions. Among the cathodic reduction current peaks, the maximum current is 5.9 mA cm^{-2}, and the current peaks of the Ag, $Ag_{90}Cu_{10}$, and $Ag_{50}Cu_{50}$ catalysts increase with increasing Cu content to approximately 3.8, 5.6, and 5.9 mA cm^{-2}, respectively. These results suggest that appropriate Cu doping is beneficial to the catalytic activities of the Ag-based alloys. Comparing the curves of the bimetallic Ag−Cu catalysts, the LSV trends of $Ag_{90}Cu_{10}$ and $Ag_{50}Cu_{50}$ are similar to that of pure Ag. However, for the $Ag_{25}Cu_{75}$ catalyst, the cathodic reduction current peak decreases to 3.1 mA cm^{-2}, and the cathodic reduction current peak almost disappears.

To investigate the effects of the pure Ag, $Ag_{90}Cu_{10}$, $Ag_{50}Cu_{50}$, and $Ag_{25}Cu_{75}$ catalysts on the ORR kinetics at different rotation rates, a set of RDE measurements were performed. As shown in Figure 3c−e and Figures S2 and Figure S3, all of the current densities increase with the rotation rate. Figure 3e presents the curves of the $Ag_{90}Cu_{10}$, $Ag_{75}Cu_{25}$, and $Ag_{50}Cu_{50}$ catalysts, which exhibit a higher limiting current density and more positive onset potential than the Ag catalyst. Furthermore, the ORR activities of the $Ag_{90}Cu_{10}$, $Ag_{75}Cu_{25}$, and $Ag_{50}Cu_{50}$ catalysts are enhanced by doping Cu atoms into Ag.

Parts f and g of Figure 3 and Figures S3c present the Koutecky−Levich plots, which are obtained from the limiting current density and calculated using eq 3. The number (n) of electrons transferred in the ORR process can be obtained from the slope of the Koutecky−Levich plot.[35,36]

$$j^{-1} = j_{\mathrm{k}}^{-1} + (0.62nFCD^{2/3}\nu^{-1/6}\omega^{1/2})^{-1} \qquad (3)$$

where j is the measured electrode current density, j_{k} is the kinetic current density, and ω is the electrode rotation rate. The value of D is 1.9×10^{-5} cm^2/s, of C is 1.2×10^{-3} mol/L, of ν is 1.1×10^{-2} cm^2/s, and of F is 96485 C/mol. From the Koutecky−Levich plots, at a potential of 0.8 V, the electron transfer numbers of the pure Ag, $Ag_{90}Cu_{10}$, $Ag_{75}Cu_{25}$, $Ag_{50}Cu_{50}$, and $Ag_{25}Cu_{75}$ catalysts are 3.4, 4, 4, 3.9, and 3.1, respectively. The OER activities of the nickel foam, $Ag_{25}Cu_{75}$ $Ag_{50}Cu_{50}$, $Ag_{75}Cu_{25}$, and $Ag_{90}Cu_{10}$ electrodes are shown in Figure 3h. As shown, the Ag−Cu alloy exhibits higher OER current density than the nickel foam at 1 V (SCE) and displays lower onset potential than the nickel foam, suggesting that the OER is enhanced by the Ag−Cu alloy. Compared to the OER performance of pure Ag, the Ag−Cu alloy also has a better OER performance, indicating the OER activity of Ag is also enhanced by alloying with Cu.

Previous work has reported that the ORR of pure Ag is primarily via the four-electron pathway and that the ORR of carbon is via the two-electron pathway in alkaline solutions.[37] The number of electrons transferred in the Ag−Mo-22 catalyst is 3.3, and the Ag−Mo-22 catalyst proceeds via a combination of the two- and four-electron pathways.[38] It is suggested that pure Ag and bimetallic Ag−Cu catalysts may exhibit similar

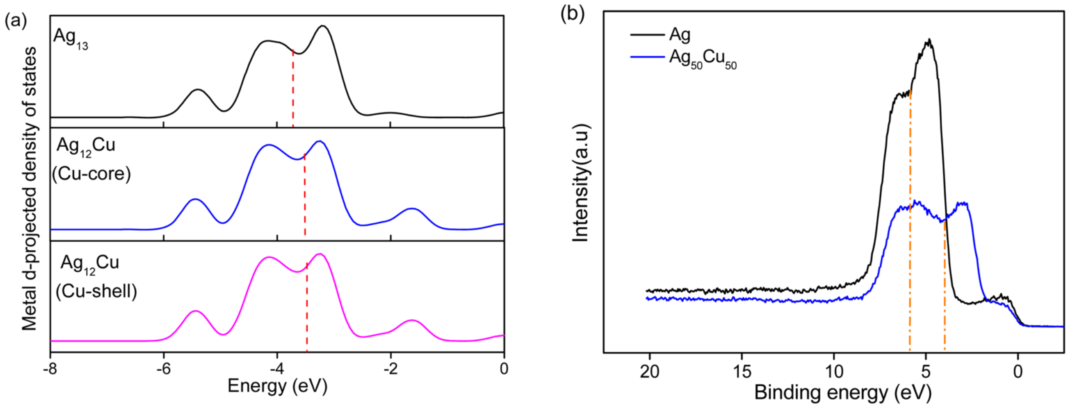

Figure 5. (a) D-projected density of states for the Ag_{13}, $Ag_{12}Cu$(Cu-core), and $Ag_{12}Cu$(Cu-shell) structures. (b) Valence band spectrum (VBS) of Ag and $Ag_{50}Cu_{50}$ alloy.

characteristics. The pure Ag catalyst with $n = 3.4$ may have both four-electron and two-electron pathways, and the four-electron pathway plays a more important role. After doping, the ORRs of the $Ag_{90}Cu_{10}$ and $Ag_{50}Cu_{50}$ catalysts follow the four-electron pathway, but with increasing Cu content, the ORRs of the $Ag_{50}Cu_{50}$ and $Ag_{25}Cu_{75}$ catalysts begin to proceed via a combined pathway with both two- and four-electron contributions. The obvious decreases in the catalytic activity of the $Ag_{25}Cu_{75}$ catalyst indicate that the excess Cu atoms changed the nature of the nanoparticles. When the Cu atoms predominate, the nanoparticles have properties that are similar to those of pure Cu. These results may explain the LSV tendency of the $Ag_{25}Cu_{75}$ catalyst to behave similarly to the Cu catalyst.

The enhanced ORR activities of the Ag−Cu nanoalloy catalysts can be understood in terms of strain and electronic effects. For the strain (or geometric) effect, the initial Ag−Cu nanoparticles have a (111) *d*-spacing that ranges from 0.220 to 0.231 nm, and the *d*-spacing is smaller than that of pure Ag, indicating that the Ag-rich nanoparticles are under compressive strain. After use, the range of the (111) *d*-spacing (ca. 0.227−0.238 nm) of the Ag-rich nanoparticles is slightly increased, suggesting that the strain effect is released during the charging and discharging processes. Therefore, strain effects enhance the ORR activity of the Ag−Cu nanoalloy catalysts.

To look into the electronic (or ligand) effects, density functional theory calculations are performed on pure Ag_{13}, $Ag_{12}Cu$(Cu-core) and $Ag_{12}Cu$(Cu-shell) clusters. The details of model and calculation methods are shown in the Supporting Information. As shown in Figure 4, the mulliken charge of silver atoms is changed by doping Cu atoms into the core or alloying them onto the surface of the $Ag_{12}Cu$ cluster. Moreover, as shown in Figure 5, the d-band center is closer to the Fermi energy level in the $Ag_{12}Cu$ cluster than in the pure Ag_{13} cluster. Table 1 lists the performance of O_2 on different adsorption sites, and it is found that the O_2 adsorption energy increases from −0.86 eV in pure Ag_{13} cluster to −1.36 eV in the $Ag_{12}Cu$ cluster (Cu-shell). Therefore, it can be inferred that alloying Cu in Ag−Cu nanoparticles thermodynamically benefits the O_2 adsorption via electronic effects.

To further determine this hypothesis, the XPS is considered to measure the valence band spectrum (VBS) of Ag and $Ag_{50}Cu_{50}$ alloy. As shown in Figure 5b, the d-band center of $Ag_{50}Cu_{50}$ is closer to the Fermi energy level than pure Ag. Obviously, as shown in Figure 3, the $Ag_{50}Cu_{50}$ catalysts exhibited a more positive onset potential and half-wave potential ($E_{1/2}$) than pure Ag catalysts. Therefore, it is clear that the ORR catalytic activity is related to the d-band center, and the ORR process could be improved by alloying Ag and Cu on the surfaces of the $Ag_{50}Cu_{50}$ nanocatalysts. So it can be concluded that the electronic (or ligand) effects play a major role for the improvement of the ORR catalytic activity in the $Ag_{50}Cu_{50}$ catalysts.

Table 1. Adsorption Energy (E_{ad}), the Electron Transfer Amount, and the Bond Length of O−O (d_{O-O}) for Each O_2 Molecular Adsorption Site on the Ag_{13}, $Ag_{12}Cu$(Cu-Core), and $Ag_{12}Cu$(Cu-Shell) Clusters

	site	E_{ad} (eV)	Mulliken charge of O_2	d_{o-o} (Å)
Ag	b	−0.52	−0.441	1.32966
	h-t	−0.86	−0.562	1.37230
	t-b-t	−0.61	−0.563	1.37209
AgCu(Cu-core)	b	−0.58	−0.438	1.32600
	h-t	−0.67	−0.629	1.40134
	t-b-t	−0.67	−0.634	1.40355
AgCu(Cu-shell)	b	−0.85	−0.662	1.41904
	h-t	−1.36	−0.661	1.40491
	t-b-t	−0.88	−0.592	1.41690

For primary zinc−air batteries, the air cathode was fabricated using $Ag_{90}Cu_{10}$ and $Ag_{50}Cu_{50}$ catalyst layers. As shown in Figure 6a, the cell voltage decreased as the current density increased and showed a strong dependence on the resistance of the battery. For the $Ag_{90}Cu_{10}$ catalysts, the open-circuit voltage of a single cell was approximately 1.44 V, the maximum power density was 82.1 mW cm^{-2}, and the battery had a 1 V voltage discharge of 50 mA cm^{-2}. For $Ag_{50}Cu_{50}$, the open-circuit voltage of the single cell was approximately 1.42 V, and the maximum power density was 86.3 mW cm^{-2}. Moreover, this battery had a 1 V voltage discharge of 60 mA cm^{-2}, which is higher than that of Ag/C[10], N-doped CNTs and silver-molybdate catalysts.[7,38,39] As shown in Figure 6b, the energy density is 896.40 mWh g^{-1}, which is 67.91% of the theoretical specific energy density (1350 mWh g^{-1}).[40]

Figure 6c presents the change in the cell voltage at 20 mA cm^{-2}. The zinc−air battery fabricated using the $Ag_{90}Cu_{10}$ catalyst had a higher initial discharge voltage (ca. 1.15 V) than that fabricated using the $Ag_{50}Cu_{50}$ catalyst (ca. 1.0 V). After 30 h of discharging, the discharge voltage of the $Ag_{90}Cu_{10}$ catalysts gradually decreased to 1.11 V, approximately 20% compared with the initial potential. Moreover, the discharge voltage of the $Ag_{50}Cu_{50}$ catalyst gradually increased to 1.18 V,

DOI: 10.1021/acsami.5b04061
ACS Appl. Mater. Interfaces 2015, 7, 17782−17791

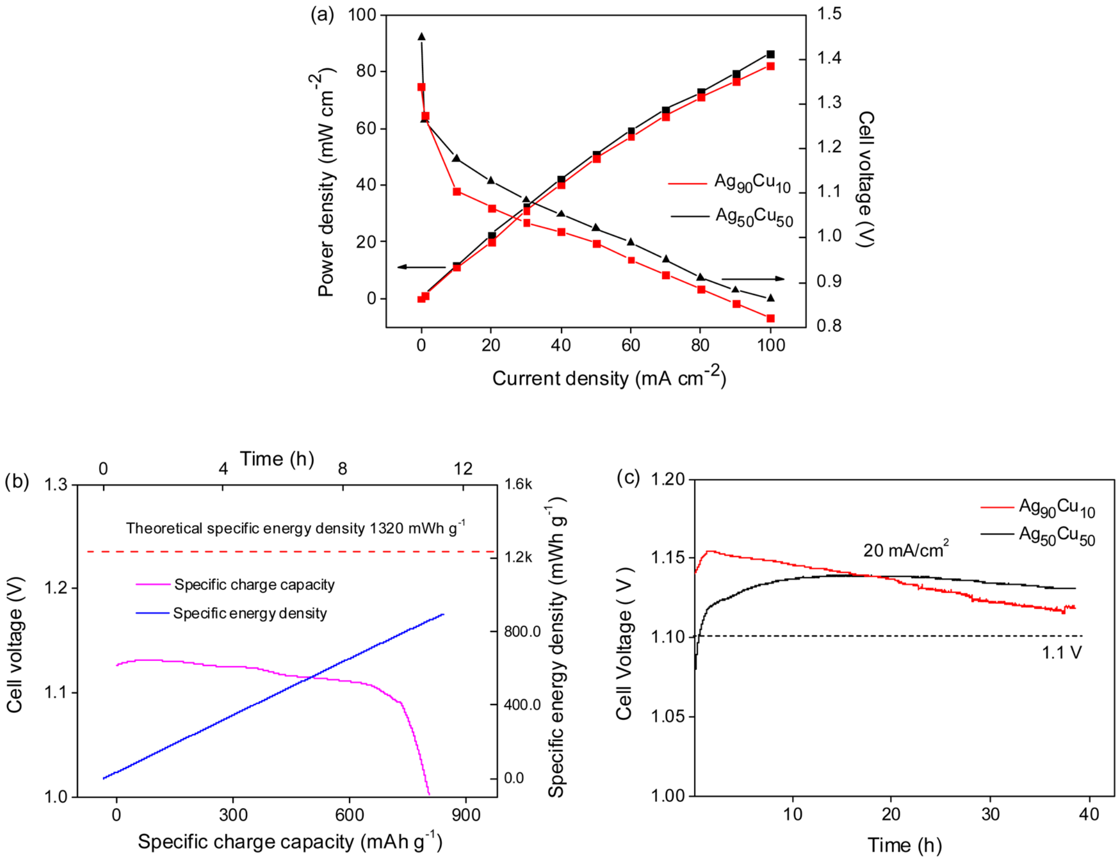

Figure 6. (a) Discharge polarization and power density curves for Ag$_{90}$Cu$_{50}$ and Ag$_{50}$Cu$_{50}$ catalyst layer for the primary zinc—air battery. (b) Specific charge capacity and specific energy density of the zinc—air battery at discharging current 20 mA cm^{-2}. (c) Voltage time curves of primary zinc—air battery at 20 mA cm^{-2}. The electrolyte is 6 M KOH solution.

approximately 16% compared with the initial potential. The Ag$_{50}$Cu$_{50}$ catalyst has higher discharge voltage stability and is more stable than the Ag$_{90}$Cu$_{10}$ catalysts for use in zinc—air batteries, appropriate Cu is a benefit for ORR.[41−43]

We also measured the charging performance and durability of the Ag—Cu-catalyzed air cathode. Figure 7a shows the charge—discharge polarization curves of the rechargeable zinc—air battery, which presents a relatively low polarization even at 100 mA cm^{-2}. Due to activation polarization, a jump is observed at the beginning of the polarization curves. After this process, the charge polarization curves show that the cell voltage increases linearly with the current density and has a maximum power density of 45.1 mW cm^{-2} at 100 mA cm^{-2}. Figure 7b shows the first-10 and last-10 cycles of the rechargeable zinc—air battery; the full cycles are shown in Figure S4. The voltage plateaus are flat and stable after charge—discharge at a current density of 20 mA cm^{-2} with 900 s/step for more than 200 cycles, and the discharge polarization increases by less than 0.01 V. The round-trip efficiency determined from Figure 7b ranges from 49.0 to 50.29% for the rechargeable zinc—air battery. For the discharging process of the rechargeable zinc—air batteries, a set of atmospheres (O$_2$, air, and N$_2$) were studied, as shown in Figure 7c. The behavior of the cathodic reaction in the atmospheres with different oxygen contents suggests that a higher oxygen concentration results in a higher discharging current. When the inlet gas is converted to pure nitrogen gas, the discharge current sharply decreases to a negligible value. During this process, no gas other than O$_2$ can be detected by gas chromatography (GC) during the discharging process. To obtain the ratio of oxygen in (oxygen consumed during battery discharge) to oxygen out (oxygen released during battery charging) at 20 mA cm^{-2}, we also measured the O$_2$ signals while charging and discharging an airtight battery (Figure S5). The O$_2$ peaks at the inlet/outlet of the battery are shown in Figure S6. During the discharging process, the oxygen peak areas are 105878, 105193, and 106531 μV s at the inlet, and the corresponding oxygen peak areas at the outlet are 102184, 101124, and 103716 μV s, respectively. Therefore, the average oxygen consumption peak area (A) is 3526 μV s. This value is the total oxygen consumption during discharging and includes all of the oxygen consumption processes from the beginning of the process. For the charging process, we employed pure N$_2$ as the standard gas, as shown in Figure S7. The released oxygen peak areas are 4068 and 3397 μV s at the outlet, and the average oxygen release peak area (A_s) is 3732 μV s. Thus, we can obtain the ratio of oxygen in/out (C) from the ratio of the consumed oxygen peak area to the released oxygen peak area (A/A_s), which is 0.945. After 1 h of discharging, the oxygen peak areas are 105477 and 104983 μV s at the inlet, and the corresponding oxygen peak areas at the outlet are 101584 and 101625 μV s. Thus, the average oxygen consumption peak area (A) is 3625.5 μV s, and the ratio of oxygen in to oxygen out is 0.973.

Figure 7d shows the discharge—charge curves of the rechargeable battery at the first, 10th, 50th, and 100th cycles. After the charge—discharge cycles, the cell voltage is decreased. The rate of decrease slows after the 10th cycle and is less than 0.006 V after the 100th cycle. This result suggests that the Ag—

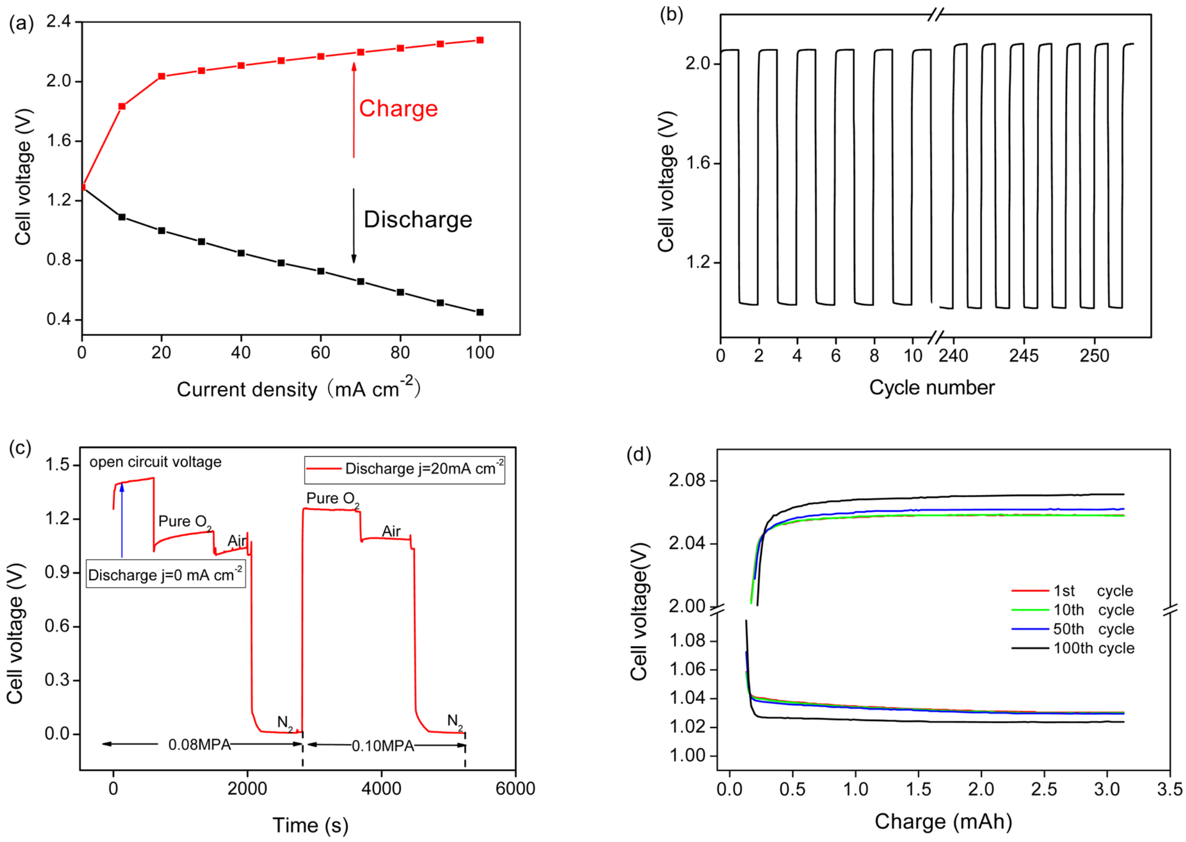

Figure 7. (a) Charge−discharge polarization curves of the rechargeable zinc−air battery. (b) First-10 and last-10 cycles of the rechargeable zinc−air battery during 252 charge−discharge cycles with period of 1800 s. (c) Discharge curves of the rechargeable zinc−air battery in O_2, air, and N_2 at 20 mA cm^{-2}. (d) Discharge−charge curves of the rechargeable zinc−air battery at the first, 10th, 50th, and 100th cycle. The current density is 20 mA cm^{-2}, and the electrolyte is 6 M KOH added with 0.1 M $Zn(CH_3COO)_2$ solution.

Cu nanoalloy catalyst layer experiences no significant degradation or corrosion during the discharge−charge process and that the Ag−Cu catalysts have a good balance between activity and durability for the zinc−air battery. Compared with the standard C/MnO_2 catalyst and other cathode catalysts for rechargeable zinc−air batteries, which are listed in Table S5, the Ag−Cu alloy catalyst layer shows a high current density (20 mA cm^{-2}) at the operating voltage of 1.08 V and a low polarization potential (0.01 V) after 200 cycles.

■ CONCLUSION

Novel bimetallic Ag−Cu nanoalloys with various Ag/Cu molar ratios were successfully synthesized using the PLD method and used as carbon-free electrocatalysts for zinc−air batteries for the first time. The nanocatalysts consist of crystalline Ag−Cu nanoalloy particles with an average size of 2.58 nm that are embedded in an amorphous Cu matrix. The Ag 3d and the Cu 2p peaks shift to higher and low binding energies in the $Ag_{50}Cu_{50}$ alloy, and the ORRs of the $Ag_{50}Cu_{50}$ and $Ag_{90}Cu_{10}$ alloys both occurred via the four-electron pathway. The resulting primary zinc−air batteries manufactured with $Ag_{50}Cu_{50}$ and $Ag_{90}Cu_{10}$ air cathodes showed that the cells have maximum power densities of 86.3 and 82.1 mW cm^{-2} at voltages of 0.863 and 0.821 V, respectively. In rechargeable zinc−air batteries, the $Ag_{50}Cu_{50}$-catalyzed air cathode required a low polarization potential to drive both the ORR and OER at 20 mA cm^{-2} and experienced no significant degradation after 200 cycles.

■ ASSOCIATED CONTENT

Ⓢ Supporting Information

The Supporting Information is available free of charge on the ACS Publications website at DOI: 10.1021/acsami.5b04061.

> Text describing additional characterization data, figures showing ORR polarization curves of Ag/Ni and $AgCu_3$/Ni, full cycle curves of the rechargeable zinc−air battery at 20 mA cm^{-2} for 200 cycles in 6 M KOH + 0.1 M $Zn(CH_3COO)_2$ solution, and details of the model and computational methods, and tables listing parameters of Koutecky−Levich plots collected from the RDE curves for pure Ag, $Ag_{75}Cu_{25}$, and $Ag_{25}Cu_{75}$ and comparison of air catalysts for zinc−air batteries (PDF)

■ AUTHOR INFORMATION

Corresponding Authors

*(F.C.) E-mail: fuyichen@nwpu.edu.cn.
*(R.L.J.) E-mail: r.l.johnston@bham.ac.uk.

Notes

The authors declare no competing financial interest.

■ ACKNOWLEDGMENTS

This study was supported by the National Natural Science Foundation of China (Grant Nos.51271148 and 50971100), the Research Fund of the State Key Laboratory of Solidification Processing in China (Grant No. 30-TP-2009), the Aeronautic Science Foundation Program of China (Grant No.

2012ZF53073), and the Doctoral Fund of the Ministry of Education of China (Grant No. 20136102110013)

■ REFERENCES

(1) Lee, J. S.; Tai Kim, S.; Cao, R.; Choi, N. S.; Liu, M.; Lee, K. T.; Cho, J. Metal-Air Batteries with High Energy Density: Li-Air versus Zn-Air. *Adv. Energy Mater.* **2011**, *1*, 34−50.

(2) Zhang, T.; Tao, Z.; Chen, J. Magnesium−Air Batteries: From Principle to Application. *Mater. Horiz.* **2014**, *1*, 196−199.

(3) Li, L.; Chai, S. H.; Dai, S.; Manthiram, A. Advanced Hybrid Li-Air Batteries with High-Performance Mesoporous Nanocatalysts. *Energy Environ. Sci.* **2014**, *7*, 2630−2636.

(4) Yang, C. Preparation and Characterization of Electrochemical Properties of Air Cathode Electrode. *Int. J. Hydrogen Energy* **2004**, *29*, 135−143.

(5) Pei, P.; Wang, K.; Ma, Z. Technologies for Extending Zinc−Air Battery's Cyclelife: A Review. *Appl. Energy* **2014**, *128*, 315−324.

(6) Liu, X.; Jia, H.; Sun, Z.; Chen, H.; Xu, P.; Du, P. Nanostructured Copper Oxide Electrodeposited from Copper(II) Complexes as an Active Catalyst for Electrocatalytic Oxygen Evolution Reaction. *Electrochem. Commun.* **2014**, *46*, 1−4.

(7) Han, J. J.; Li, N.; Zhang, T. Y. Ag/C Nanoparticles as an Cathode Catalyst for a Zinc-Air Battery With a Flowing Alkaline Electrolyte. *J. Power Sources* **2009**, *193*, 885−889.

(8) Lim, E. J.; Choi, S. M.; Seo, M. H.; Kim, Y.; Lee, S.; Kim, W. B. Highly Dispersed Ag Nanoparticles on Nanosheets of Reduced Graphene Oxide for Oxygen Reduction Reaction in Alkaline Media. *Electrochem. Commun.* **2013**, *28*, 100−103.

(9) Han, X.; Cheng, F.; Zhang, T.; Yang, J.; Hu, Y.; Chen, J. Hydrogenated Uniform Pt Clusters Supported on Porous CaMnO(3) as a Bifunctional Electrocatalyst for Enhanced Oxygen Reduction and Evolution. *Adv. Mater.* **2014**, *26*, 2047−2051.

(10) Maheswari, S.; Sridhar, P.; Pitchumani, S. Pd−TiO_2/C as a Methanol Tolerant Catalyst for Oxygen Reduction Reaction in Alkaline Medium. *Electrochem. Commun.* **2013**, *26*, 97−100.

(11) Velraj, S.; Zhu, J. H. $Sm_{0.5}Sr_{0.5}CoO_3-\delta$ − A New Bi-functional Catalyst for Rechargeable Metal-Air Battery Applications. *J. Power Sources* **2013**, *227*, 48−52.

(12) Zhang, S. S.; Read, J. Partially Fluorinated Solvent as a Co-solvent for the Non-aqueous Electrolyte of Li/air Battery. *J. Power Sources* **2011**, *196*, 2867−2870.

(13) Zhu, C.; Nobuta, A.; Nakatsugawa, I.; Akiyama, T. Solution Combustion Synthesis of $LaMO_3$(M = Fe, Co, Mn) Perovskite Nanoparticles and the Measurement of Their Electrocatalytic Properties for Air Cathode. *Int. J. Hydrogen Energy* **2013**, *38*, 13238−13248.

(14) Yu, L.; Shen, Y.; Huang, Y. Fe-N-C Catalyst Modified Graphene Sponge as a Cathode Material for Lithium-Oxygen Battery. *J. Alloys Compd.* **2014**, *595*, 185−191.

(15) Ito, A.; Zhao, L.; Okada, S.; Yamaki, J. I. Synthesis of Nano-Fe3O4-Loaded Tubular Carbon Nanofibers and Their Application as Negative Electrodes for Fe/air Batteries. *J. Power Sources* **2011**, *196*, 8154−8159.

(16) Wu, Q.; Jiang, L.; Qi, L.; Wang, E.; Sun, G. Electrocatalytic Performance of Ni Modified MnO_x/C Composites Toward Oxygen Reduction Reaction and Their Application in Zn−air Battery. *Int. J. Hydrogen Energy* **2014**, *39*, 3423−3432.

(17) Ma, J.; Wen, J.; Gao, J.; Li, Q. Performance of Al−0.5 Mg−0.02 Ga−0.1 Sn−0.5 Mn as Anode for Al−air Battery in NaCl Solutions. *J. Power Sources* **2014**, *253*, 419−423.

(18) Kwon, E.; Lim, H. S.; Sun, Y. K.; Suh, K. D. Improved Rate Capability of Lithium-ion Batteries with Ag Nanoparticles Deposited onto Silicon/Carbon Composite Microspheres as an Anode Material. *Solid State Ionics* **2013**, *237*, 28−33.

(19) Lima, F. H. B.; de Castro, J. F. R.; Ticianelli, E. A. Silver-Cobalt Bimetallic Particles for Oxygen Reduction in Alkaline Media. *J. Power Sources* **2006**, *161*, 806−812.

(20) Slanac, D. A.; Hardin, W. G.; Johnston, K. P.; Stevenson, K. J. Atomic Ensemble and Electronic Effects in Ag-rich AgPd Nanoalloy Catalysts for Oxygen Reduction in Alkaline Media. *J. Am. Chem. Soc.* **2012**, *134*, 9812−9891.

(21) Tang, H.; Tang, Z.; Du, C.; Qie, F.; Zhu, J. Ag-Doped $Li_2ZnTi_3O_8$ as a High Rate Anode Material for Rechargeable Lithium-ion Batteries. *Electrochim. Acta* **2014**, *120*, 187−192.

(22) Ma, W.; Chen, F.; Zhang, N.; Wu, X. Oxygen Reduction Reaction on Cu-Doped Ag Cluster for Fuel-Cell Cathode. *J. Mol. Model.* **2014**, *20*, 2454−2461.

(23) Shin, K.; Kim, D. H.; Yeo, S. C.; Lee, H. M. Structural Stability of AgCu Bimetallic Nanoparticles and Their Application as a Catalyst: A DFT study. *Catal. Today* **2012**, *185*, 94−98.

(24) Kanoun, M. B.; Cavallo, L. Quantifying the Impact of Relativity and of Dispersion Interactions on the Activation of Molecular Oxygen Promoted by Noble Metal Nanoparticles. *J. Phys. Chem. C* **2014**, *118*, 13707−13714.

(25) Sheng, H.; He, J.; Ma, E. Molecular Dynamics Simulation Studies of Atomic-Level Structures in Rapidly Quenched Ag-Cu Nonequilibrium Alloys. *Phys. Rev. B: Condens. Matter Mater. Phys.* **2002**, *65*, 184203.

(26) Lu, Y.; Zhang, N.; An, L.; Li, X.; Xia, D. Synthesis of High Dispersed Intermetallic Ag_4Sn/C and Its Enhanced Oxygen Reduction Reaction Activity. *J. Power Sources* **2013**, *240*, 606−611.

(27) Liu, Y.; Jordan, R.; Qiu, S. Electronic Structures of Ordered Ag-Mg Alloys. *Phys. Rev. B: Condens. Matter Mater. Phys.* **1994**, *49*, 4478−4484.

(28) Tyson, C.; Bzowski, A.; Kristof, P.; Kuhn, M.; Sammynaiken, R.; Sham, T. Charge Redistribution in Au-Ag alloys from a Local Perspective. *Phys. Rev. B: Condens. Matter Mater. Phys.* **1992**, *45*, 8924−8928.

(29) Schaal, M. T.; Hyman, M. P.; Rangan, M.; Ma, S.; Williams, C. T.; Monnier, J. R.; Medlin, J. W. Theoretical and Experimental Studies of Ag−Pt Interactions for Supported Ag−Pt Bimetallic Catalysts. *Surf. Sci.* **2009**, *603*, 690−696.

(30) Gonzalo, J.; Babonneau, D.; Afonso, C. N.; Barnes, J. P. Optical Response of Mixed Ag-Cu Nanocrystals Produced by Pulsed Laser Deposition. *J. Appl. Phys.* **2004**, *96*, 5163−5168.

(31) Langlois, C.; Li, Z. L.; Yuan, J.; Alloyeau, D.; Nelayah, J.; Bochicchio, D.; Ferrando, R.; Ricolleau, C. Transition from Core-Shell to Janus Chemical Configuration for Bimetallic Nanoparticles. *Nanoscale* **2012**, *4*, 3381−3388.

(32) John, F. M.; William, F. S.; Peter, E. S.; Kenneth, D. B. *Handbook of X-ray Photoelectron Spectroscopy*. Perkin-Elmer Corporation Physical Electronics Division: Eden Prairie, Minnesota, USA, 1992; p 261.

(33) Knight, J. M.; Fonseca, J. L. C.; Hauptman, Z. V.; Badyal, J. P. S. Novel Surface Segregation Phenomena at the Plasma/Copper-Silver Alloy Interface. *Chem. Mater.* **1993**, *5*, 1221−1226.

(34) Chen, F.; Johnston, R. L. Charge Transfer Driven Surface Segregation of Gold Atoms in 13-Atom Au−Ag Nanoalloys and Its Relevance to their structural, optical and electronic properties. *Acta Mater.* **2008**, *56*, 2374−2380.

(35) Meng, H.; Shen, P. K. Novel Pt-free Catalyst for Oxygen Electroreduction. *Electrochem. Commun.* **2006**, *8*, 588−594.

(36) Tammeveski, L.; Erikson, H.; Sarapuu, A.; Kozlova, J.; Ritslaid, P.; Sammelselg, V.; Tammeveski, K. Electrocatalytic Oxygen Reduction on Silver Nanoparticle/multi-walled Carbon Nanotube Modified Glassy Carbon Electrodes in Alkaline Solution. *Electrochem. Commun.* **2012**, *20*, 15−18.

(37) Garcia, A. C.; Gasparotto, L. H. S.; Gomes, J. F.; Tremiliosi-Filho, G. Straightforward Synthesis of Carbon-Supported Ag Nanoparticles and Their Application For the Oxygen Reduction Reaction. *Electrocatalysis* **2012**, *3*, 147−152.

(38) Wang, Y.; Liu, Y.; Lu, X.; Li, Z.; Zhang, H.; Cui, X.; Zhang, Y.; Shi, F.; Deng, Y. Silver-Molybdate Electrocatalysts for Oxygen Reduction Reaction in Alkaline Media. *Electrochem. Commun.* **2012**, *20*, 171−174.

(39) Zhu, S.; Chen, Z.; Li, B.; Higgins, D.; Wang, H.; Li, H.; Chen, Z. Nitrogen-Doped Carbon Nanotubes as Air Cathode Catalysts in Zinc-air Battery. *Electrochim. Acta* **2011**, *56*, 5080−5084.

(40) Goldstein, J.; Brown, I.; Koretz, B. New Developments in the Electric Fuel Ltd Zinc Air System. *J. Power Sources* **1999**, *80*, 171−179.
(41) Kim, J. K.; Yang, W.; Salim, J.; Ma, C.; Sun, C.; Li, J.; Kim, Y. Li-Water Battery with Oxygen Dissolved in Water as a Cathode. *J. Electrochem. Soc.* **2013**, *161* (3), A285−A289.
(42) Yang, W.; Salim, J.; Li, S.; Sun, C.; Chen, L.; Goodenough, J. B.; Kim, Y. Perovskite Sr0.95Ce0.05CoO3−δ Loaded with Copper Nanoparticles as a Bifunctional Catalyst for Lithium-Air Batteries. *J. Mater. Chem.* **2012**, *22* (36), 18902−18907.
(43) Yang, W.; Salim, J.; Ma, C.; Ma, Z.; Sun, C.; Li, J.; Chen, L.; Kim, Y. Flowerlike Co3O4Microspheres Loaded with Copper Nanoparticle as an Efficient Bifunctional Catalyst for Lithium−Air Batteries. *Electrochem. Commun.* **2013**, *28*, 13−16.